Title:

Detection of Cracks with Arbitrary Orientations in a Metal Pipe Using Linearly-Polarized Circular TE_{11} Mode Microwaves

Authors:

Guanren Chen*, Takuya Katagiri, Haicheng Song, Noritaka Yusa, Hidetoshi Hashizume

Affiliation:

Department of Quantum Science and Energy Engineering, Graduate School of Engineering, Tohoku University, 6-6-01-2, Aramaki Aza Aoba, Aoba, Sendai, Miyagi 980-8579, Japan

Corresponding author:

Guanren Chen

Tel/Fax: +81-22-7957906

email: chen.guanren.q8@dc.tohoku.ac.jp

Abstract

This study proposed a long-range non-destructive pipe inspection approach using linearly-polarized circular TE_{11} mode microwaves, enabling rapid detection of both axial and circumferential cracks on the inner surface of a metallic pipe. The applicability of the TE_{11} mode microwaves for crack detection was discussed in the light of the currents induced on the inner surface of a pipe due to the propagation of the TE_{11} mode microwaves. A dual-bend structured mode converter was designed to propagate linearly-polarized TE_{11} mode microwaves inside a pipe with a certain inner diameter, based on the theoretical and numerical analysis of mode conversion due to a bend. A 3.5 GHz working bandwidth of the mode converter was achieved with a conversion efficiency of the TE_{11} mode of over 90%. Experimental verification was conducted using stainless-steel pipes with an inner diameter of 23 mm and a total length of 7 m. An axial and a circumferential slit were introduced to simulate cracks. The experimental results confirmed reflections from both the axial and circumferential slits, indicating that the TE_{11} mode microwaves are applicable to crack detection. The results also confirmed the correlation between TE_{11} mode polarization and its detection sensitivity toward slits with different orientations along the circumferential direction. Furthermore, the axial and circumferential slits situated at different longitudinal and circumferential locations in the pipe were successfully detected by orthogonally deploying the mode converter to change the polarization of the TE_{11} mode by 90 degrees.

Keywords: TE_{11} mode, microwaves, NDT, mode converter, crack detection

1. Introduction

Maintenance of large-scale and complicated piping systems has always been a challenging task [1-4]. It is often limited by the space available, the circumstances of operation or the installation of the inspection device. On the other hand, it requires high reliability, speed and precision of inspection. Eddy current testing [5-8] and ultrasonic testing [9-12] have been used for the inspection of piping systems, and have proved to possess high accuracy. However, these methods require surface preparation and a surface scan, which considerably reduces the inspection efficiency and restricts usage of those inspection methods.

Microwave non-destructive testing (NDT) [13-16], as a state-of-the-art pipe inspection technology, can realize the detection and location of flaws inside pipes efficiently and remotely. This method propagates microwaves in a metallic pipe, and measures reflections of the microwaves caused by flaws on the inner surface of the pipe. Because microwaves propagate inside pipes at almost light speed with very low attenuation, this method has the capability to realize rapid inspection of a long-range pipeline system. Some previous studies [17-19] have demonstrated the effectiveness of microwave NDT in detecting pipe wall thinning. Also, a recent study [20] reported that a detection range of over 20 m was achieved by applying this method, when a full-circumferential artificial pipe wall thinning was used as the flaw.

Contrary to the pipe wall thinning, cracks, as one of the most typical degradations of pipes, are more difficult to detect, not only because of their smaller size, but also because the orientations of cracks significantly influence the detection sensitivity of the microwave NDT. For instance, TM_{01} mode microwaves are susceptible to circumferential cracks [21] but insusceptible to the axial slits. In contrast, TE_{01} mode microwaves are sensitive to axial cracks but insensitive to circumferential ones [22]. The orientated sensitivity of a microwave mode limits the use of microwave NDT for pipe inspection and lowers the detection efficiency. In order to overcome this limitation, a new testing method is anticipated to be developed.

This research targeted the development of a pipe inspection approach using linearly-polarized TE_{11} mode microwaves, which enables the detection of both axial and circumferential cracks in a pipe. The rest of this paper is organized as follows. In Section 2, the feasibility of adopting TE_{11} mode microwaves for crack detection was discussed, and the relationship between the TE_{11} mode polarization and its detection sensitivity against slits with different orientations was also studied. In Section 3, a systematic method was developed to design a dual-bend TE_{11} mode converter for a certain pipe inner diameter, with the aid of theoretical computation and numerical simulation. In Section 4, experimental verification was carried out using a 7 m long straight pipe with an inner diameter of 23 mm, while an axial and a circumferential slit were introduced to simulate cracks. The experimental result showed clear reflection signals from the axial and circumferential slits, which proved the detection capability of TE_{11} mode microwaves for cracks. In addition, the orthogonal deployment of the mode converter, which changed the polarization of TE_{11} mode by 90 degrees, allowed the detection of both axial and circumferential slits located at arbitrary longitudinal or circumferential positions with a high sensitivity.

2. Detecting a crack using TE_{11} mode microwaves

When an electromagnetic wave propagates in a metallic pipe, current $\boldsymbol{J}_s$ is induced on the inner surface of the pipe. In general, the sensitivity of microwave NDT against a flaw can be explained in terms of the disturbance of $\boldsymbol{J}_s$ caused by the flaw. Actually, an earlier study [21] of the authors demonstrated that TM_{01} mode microwaves, which induce $\boldsymbol{J}_s$ in the axial direction, are sensitive to a circumferential slit, whereas they are insensitive to an axial slit. Another recent study [22] of the authors has verified that TE_{01} mode, which induces $\boldsymbol{J}_s$ in the circumferential direction, has a good sensitivity to an axial slit but poor sensitivity to a circumferential one. Figure 1 shows the amplitudes of reflection signals when TM_{01} mode microwaves were utilized for detecting axial and circumferential slits of different surface length, respectively [23]. As shown in the figure, the amplitude of reflection signal changes significantly along with the size of circumferential slit, but maintains almost unchanged with the size of axial slit increasing. The above discussion on the relationship between $\boldsymbol{J}_s$ and detection sensitivity as well as the result shown in the figure implies that: TM_{01} or TE_{01} mode microwaves only possess the sensibility against the circumferential or axial crack, and remains insensitive to the other; on the other hand, the linearly-polarized TE_{11} mode, containing both circumferential and axial component of $\boldsymbol{J}_s$, may enables us to detect axial and circumferential flaws as explained below.

Figure 2(a) shows the electromagnetic field and surface current distribution of linearly-polarized TE_{11} mode microwaves. By convention, the 'polarization' of electromagnetic waves refers to the direction of the electric field, which indicates that the polarization shown in the figure is defined as horizontal polarization. Based on the aforementioned discussions on the relationship between detection sensitivity and $\boldsymbol{J}_s$, an axial flaw located at points A or C will disturb the flow of $\boldsymbol{J}_s$ and generate a reflection signal for detection. Meanwhile, a circumferential flaw located at points B or D will disturb the $\boldsymbol{J}_s$ flow and generate a detectable reflection signal, as shown in Fig.2 (b). In the other areas, not only axial but also circumferential flaws can be detected. By contrast, the employment of vertically polarized TE_{11} mode microwaves, displayed in Fig. 3(a), would lead to a high sensitivity against circumferential flaws at points A or C and axial flaw at points B or D, as shown in Fig.3 (b). This indicates that the polarization of the TE_{11} mode determines the detection sensitivity to flaws with different orientations in the circumferential direction. Additionally, since the sensitive areas of horizontal or vertical polarization exactly overlap the detection dead zone of each other, a joint analysis of reflection signals under two polarizations would make both axial and circumferential flaws become detectable despite their circumferential positions in a pipe.

3. Design of the TE_{11} mode converter

The structure of the TE_{11} mode converter used in this study is illustrated in Fig. 4. It encompasses a TEM-TM_{01} mode converter and a TM_{01}-TE_{11} mode converter, consisting of two inversely connected bends. Actually, the dual-bend TM_{01}-TE_{11} mode converter or a similar type was proposed and developed in several previous studies [24-27] for high power microwave systems. However, most of them were dedicated to work at a certain center frequency with a relatively narrow operating frequency range. In the case of microwave NDT, the inner diameter of the pipe under test is the main factor, while a wider working bandwidth is preferable for a higher time domain resolution [28-30]. Moreover, these studies mainly concentrated on the conversion from TM_{01} to TE_{11} mode but paid little attention to the excitation of the TM_{01} mode. In this study, the TE_{11} mode converter was systematically designed using the following steps: (1) Design the TEM-TM_{01} mode converter for a designated pipe inner diameter D by means of numerical simulation, and obtain the operational frequency range of TM_{01} mode; (2) Over the obtained frequency range, calculate the fractional energy of each mode on the condition that TM_{01} mode microwaves propagate through the dual-bend TM_{01}-TE_{11} mode converter, based on the theory of mode conversion due to a bend; (3) In terms of the theoretically calculated results, optimize the dimensions of the dual-bend TM_{01}-TE_{11} mode converter.

3.1 Design of the TEM-TM_{01} mode converter

The TEM-TM_{01} mode converter was designed on the basis of a former study [31]. The structure of the mode converter is shown in Fig. 5 (a). A semi-rigid cable (Anritsu Corporation, K118) was attached to the center of a plate cap with a standard ferrule connection (the full-circumferential groove with a diameter of 43.5 mm on the plate). A connector (Anritsu Corporation, K101F-R) fixed to one end of the cable was used for connection. Part of the core wire was exposed for an optimum length in order to achieve a higher efficiency of conversion from TEM-to TM_{01} mode. In this study, the pipe's inner diameter D was set to 23 mm, while the exposure length of the core wire was set to 6 mm, which was determined by the results of the numerical simulations. Figure 5(b) reveals the reflection and transmission characteristics of the TEM-TM_{01} mode converter. The operational frequency range of the TM_{01} mode was from 10.3 to 16.3 GHz, within which the energy ratio of the converted TM_{01} mode was over

50%. The conversion from TM_{01} to TE_{11} mode over this frequency range will be evaluated hereafter.

3.2 Dual-bend TM_{01}-TE_{11} mode converter

3.2.1 Mode conversion of microwaves due to a bend

The conversion from the TM_{01} to TE_{11} mode is computed based on the principle of mode conversion due to a bend. This theory was proposed in several early studies [32-34] and is given as the following equation system:

$$\begin{cases} \dfrac{\mathrm{d}A^{+}_{m'n'}}{\mathrm{d}z} = -\mathrm{j}\beta_{m'n'}A^{+}_{m'n'} - \mathrm{j}\sum_{mn} C^{\pm}_{(m'n')(mn)}A^{\pm}_{mn} \\ \dfrac{\mathrm{d}A^{-}_{m'n'}}{\mathrm{d}z} = \mathrm{j}\beta_{m'n'}A^{-}_{m'n'} + \mathrm{j}\sum_{mn} C^{\pm}_{(m'n')(mn)}A^{\mp}_{mn} \end{cases}, \quad (1)$$

where A, C and β denote the complex amplitude of the coupled mode, coupling coefficient and phase constant, respectively. Subscripts m, n, m' and n' are mode numbers, bound by $|m - m'| = 1$. Signs '+' and '-' refer to the forward direction and backward direction of propagation. The length of the bend is z, and $z = r\cdot\alpha$, in which r and α are the curvature radius of the bend and bend angle, corresponding to Fig. 4. The expressions of the coupling coefficient C among different modes were also given in the early studies [32-34], while C depends on r, D and frequency f. Meanwhile, the phase constant β hinges on D and f. Therefore, it is obvious that the mode conversion at a bend is dependent on four factors: r, D, f and α, when the coupled modes are determined. Now we shall calculate the mode conversion of the TM_{01} mode microwaves when it propagates through the dual-bend TM_{01}-TE_{11} mode converter. First of all, to calculate the mode conversion at a single bend over a certain frequency span, we first need to determine the coupled modes. That is because aside from the desired conversion from TM_{01}

to TE_{11} mode, there are also several spurious modes generated in the mode coupling. When D = 23 mm, over the operational frequency range of the TM_{01} mode given in Section 3.1 (10.3 – 16.3 GHz), a total of four propagating modes were involved in the calculation of the mode conversion. They are TE_{11}, TM_{01}, TE_{21} and TM_{11} mode, and their cut-off frequencies are 7.64, 9.98, 12.68 and 15.91 GHz, respectively. It should be noted that the TE_{01} mode needs to be excluded even though its cut-off frequency is within the input frequency range. Because the preliminary simulation results showed that the TE_{01} mode could not be generated in the mode coupling when TM_{01} mode was the only excitation mode. The mode coupling among the above mentioned four modes to the forward direction was calculated as:

$$\frac{\mathrm{d}}{\mathrm{d}\alpha}\begin{pmatrix} A_1 \\ A_2 \\ A_3 \\ A_4 \end{pmatrix} = -\mathrm{j}\begin{pmatrix} r\beta_1 & rC_{12} & rC_{13} & rC_{14} \\ rC_{21} & r\beta_2 & rC_{23} & rC_{24} \\ rC_{31} & rC_{32} & r\beta_3 & rC_{34} \\ rC_{41} & rC_{42} & rC_{43} & r\beta_4 \end{pmatrix}\begin{pmatrix} A_1 \\ A_2 \\ A_3 \\ A_4 \end{pmatrix}, \quad (2)$$

where subscripts 1 – 4 refer to modes TE_{11}, TM_{01}, TE_{21}, and TM_{11}, C_{ij} (i, j=1 – 4) denotes the coupling coefficient among four modes, and $C_{ij} = C_{ji}$. When the two coupled modes do not fulfill the condition $|m - m'| = 1$, their coupling coefficient C_{ij} is 0. The initial value is set to $\boldsymbol{A}_0$= [0,1,0,0] $^{\mathrm{T}}$. The solution of Eq. (2) is the result of mode conversion of a single bend. To calculate the mode conversion of two inversely connected bends, we should proceed as follows. Firstly, calculate Eq. (2) and obtain the output of first bend; secondly, replace the r and α in Eq. (2) with $-r$ and $-\alpha$; finally, calculate Eq. (2) again utilizing the result of the first step as the initial value. Note that the calculated result $\boldsymbol{A} = [A_1, A_2, A_3, A_4]^{\mathrm{T}}$ is a vector of complex amplitudes, while the fractional energy of each mode is the square of absolute value of $\boldsymbol{A}$.

According to the authors' previous works [35,36], the mode conversion at a bend is actually dependent on three factors: r/D, α and the normalized frequency f/f_c, wherein f_c is the cut-off frequency of an arbitrary mode. It simplifies the calculation of mode conversion by reducing the number of parameters, and merges similar cases. This conclusion will be adopted in the next section to optimize the dimensions of the TM_{01}-TE_{11} mode converter.

3.2.2 Dimensional optimization of the dual-bend TM_{01}-TE_{11} mode converter

As interpreted at the beginning of Section 3, the working bandwidth of the mode converter ought to be as wide as possible so as to obtain a higher time domain resolution. Since the operational frequency range of the TM_{01} mode has been given in Section 3.1, if using the cut-off frequency of TM_{01} mode f_{cM01} for normalization, the normalized operational frequency span of TM_{01} mode f/f_{cM01} was calculated as 1.03 – 1.63. Therefore, an optimum combination of r/D and α should be selected for the dual-bend TM_{01}-TE_{11} mode converter to maximize working bandwidth over the given range of f/f_{cM01}. This study defines the working bandwidth as the frequency range within which the energy ratio of TE_{11} mode is greater than or equal to 90%. In order to simplify the calculation, the curvature radii r and bend angles α of two bends of the mode converter were set to identical. Then, r/D and α were scanned in terms of the values listed in Table 1 to calculate the normalized working bandwidth of the converted TE_{11} mode.

Figure 6 (a) depicts the computational results of normalized working bandwidth for the r/D & α group in Table 1. As shown in the figure, the maximum normalized working bandwidth was 0.35, acquired when $r/D = 2.6$ & $\alpha = 51°$ or $r/D = 2.7$ & $\alpha = 49°$. Figure 6 (b) shows the theoretically calculated results of one scenario ($r/D = 2.6$ & $\alpha = 51°$). The energy ratio of TE_{11} mode was greater than or equal to 90% when f/f_{cM01} ranged from 1.24–1.59. The calculated result of another scenario ($r/D = 2.7$ & $\alpha = 49°$) was similar to the result displayed in Fig. 6 (b), enabling us to discuss only one of them.

Three-dimensional finite element simulations were also performed for verification, adopting COMSOL Multiphysics v5.0 with the RF module. The governing equation is:

$$\nabla\times\mu_r^{-1}(\nabla\times\boldsymbol{E})-k_0^2[\varepsilon_r-\mathrm{j}\sigma/(\omega\varepsilon_0)]\boldsymbol{E}=0, \quad (3)$$

where $k_0=\omega\sqrt{\varepsilon_0\mu_0}$ is the propagation constant in a vacuum, ε_0 and μ_0 are permittivity and permeability in a vacuum, ω is the angular frequency, and j is the imaginary unit. Vector $\boldsymbol{E}$ denotes electric field, and σ is the electrical conductivity. Variables ε_r and μ_r are relative permittivity and relative permeability. In this computation, the values are: $\mu_r=1$, $\varepsilon_r=1.000$ and $\sigma=0$, for the media air.

The geometrical model is illustrated in Fig. 7 (a). The inner diameter of the pipe, *D*, is 23 mm, while the curvature radius *r* and bend angle α are set to 60 mm ($r/D\approx2.6087$) and 51°, respectively. TM_{01} mode microwaves were excited at one end of the model (surface I), while the transmission characteristics of converted modes were evaluated at the surface II. A perfectly matched layer (PML) was placed at the other end to eliminate the reflection at the surface. Second-order tetrahedral were used for discretization. The sweeping frequency span was from 12.0 GHz to 16.0 GHz, with a step of 0.1 GHz.

Figure 7 (b) describes the comparison between theoretical calculation and numerical simulation. The theoretically calculated energy ratio of each mode was consistent with that of numerical simulation. The working bandwidth of the dual-bend TE_{11} mode converter was 3.5 GHz, approximately ranging from 12.4 to 15.9 GHz.

4. Experiment

4.1 Experimental setup

Figure 8 (a) shows an overview of the experimental system of this study. A network analyzer (Agilent Technologies, E8363B) was utilized to emit coaxial TEM mode microwaves. The excited microwaves were subsequently propagated into a flexible cable (Junkosha. Inc., MWX051) and converted into circular TM_{01} mode by the TEM-to-TM_{01} mode converter (narrated in 3.1). Then the TM_{01} mode was further converted into linearly-polarized TE_{11} mode by the dual-bend TM_{01}-TE_{11} mode converter or directly emitted into the pipe by changing the connection layout of mode converters as illustrated in Fig. 8 (b), (c) and (d).

A seven-meter long metal pipe was used for testing. The pipe's material was type 304 stainless-steel pipe. Given that it is difficult to prepare a seamless pipe with a long distance, seven short pipes with a length of 1 m were used and connected with ferrule connections (ISO sanitary ferrule fitting, 1" or 1.0S, Osaka Sanitary Co., Ltd). The inner diameter and wall thickness of the pipes were 23 mm and 1.2 mm, respectively. A tailored O-ring and two rubber mats were installed at every ferrule connection to eliminate misalignment in the pipe connections and reduce the reflection from the connections. The photo of experimental setup is exhibited in Fig. 9.

To simulate cracks in a pipe, an axial slit and a circumferential slit were fabricated by a machine saw in the middle of two pipes. The slits were longitudinally deployed at L_S = 1.5 m, 3.5 m and 5.5 m, and circumferentially situated at four points, A, B, C and D as shown in the dash line box in Fig.8 (a). The profile and dimensions of the two types of slits are illustrated in Fig. 10 (a) and (b). Table 2 summarizes the details of the deployments of the two slits.

The frequency range used in the experiments was 12.4-15.9 GHz in accordance with the results in Section 3.2.2. The microwave reflections were measured at 3201 uniformly-spaced frequencies, with an average of 30 measurements. Afterwards, the measured frequency-domain signals were converted into the time domain using inverse Fourier transform with a Kaiser window function (n = 6).

4.2 Results and discussion

Figures 11 and 12 present the time domain reflection signals of the axial and circumferential slits situated at L_S = 3.5 m, when the propagating modes are TE_{11} mode of horizontal polarization and vertical polarization, respectively. In each figure, the high reflection peak near 0 ns is from the TEM-to-TM_{01} mode converter, while the reflection appearing at around 59 ns corresponds to the pipe end (7 m). There is another discernible reflection peak appearing at about 3.5 ns, corresponding to the outlet of the TM_{01}-TE_{11} mode converter, namely the inlet of the pipe. Reflection signals due to slits are highlighted with down-arrows. As shown in Fig. 11, reflections due to the axial slits at points A and C and circumferential slits at points B and D were clearly observed at 31 ns or so, which accords with the analysis of sensitive areas in Fig. 2. Similarly, in Fig. 12, axial slits at points B and D and circumferential slits at points A and C were also explicitly detected, corresponding to Fig. 3. There are several local reflection peaks from about 10 ns to 55 ns, which were caused by the ferrule connections. On the basis of the above discussions, it can be concluded that: orthogonally deploying the TM_{01}-to-TE_{11} mode converter to change the polarization of TE_{11} mode, along with jointly analyzing the reflection signals under two polarizations, enables us to detect both axial and circumferential slits located at arbitrary circumferential positions.

Figure 13 shows the time domain reflection signals when the TM_{01} mode was used for testing, while the slits were also situated at L_s = 3.5 m. Similarly, the reflection peaks at around 0 ns and 67 ns correspond to the TEM-to-TM_{01} mode converter and the pipe end. The local reflection peaks from about 10 to 60 ns were also caused by the ferrule connections, and they are a little bit larger than the reflections caused by ferrule connections in Fig. 11 and 12. That is because that the surface current of the TM_{01} mode is longitudinal, which makes it more susceptible to the circumferential anomaly inside the pipe. The discernible reflections resulting from the slits are also marked with down-arrows. Comparing (a)–(d) with (e)–(h) in Fig. 13, although the TM_{01} mode showed an all-around sensitivity to circumferential slits, it had zero detectability of axial slits.

A signal-processing method [37] was adopted to compensate the dispersion of measured signals and predict the positions of slits. Figures 14 and 15 show the processed reflection signals of the axial and circumferential slits listed in Table 2, respectively. The results indicate that either axial or circumferential slits situated at L_S = 1.5 m, 3.5 m, 5.5 m and four different circumferential positions can be effectively detected and located, employing the TE_{11} mode microwaves of the two orthogonal polarizations. Small localized peaks appearing at 1 m, 2 m ..., 7 m correspond to the ferrule connections. The results demonstrated the viability of using linearly-polarized TE_{11} mode microwaves to detect slits with arbitrary orientations in a pipe.

5. Conclusion

This research validated the applicability of the linearly-polarized circular TE_{11} mode microwaves for the detection of cracks located on the inner surface of a pipe with arbitrary orientations. Both axial and circumferential slits, deployed in a 7 m straight pipe to simulate a crack, were detected by use of a dual-bend TE_{11} mode converter, which was designed for inspecting the pipe of a certain inner diameter. The experimental results also indicated that the linearly-polarized TE_{11} mode microwave's detection sensitivity to cracks with different orientations in a circumferential direction is dependent on its polarization. Therefore, an orthogonal deployment of the mode converter, comprising the horizontal as well as vertical polarization, can eliminate the detection dead zones of either polarization and realize the detection of either axial or circumferential slits situated at arbitrary longitudinal/circumferential positions in a pipe.

Acknowledgment

This study was partially supported by Grant-in-Aid for JSPS fellows (No. 18J20649). The authors appreciate the assistance of the mechanical fabrication provided by Mr. Takao Nagaya, affiliated with the School of Engineering, Tohoku University. The authors also would like to thank the China Scholarship Council (CSC) for its financial support of the stipend to the first author.

Reference

[1] Liu Z, Kleiner Y. State-of-the-art review of technologies for pipe structural health monitoring. IEEE Sensors Journal. 2012;12(6):1987-1992.

[2] Eason, Thomas J., Leonard J. Bond, and Mark G. Lozev. Structural health monitoring of localized internal corrosion in high temperature piping for oil industry. In AIP Conference Proceedings, vol. 1650, no. 1, pp. 863-873. AIP, 2015.

[3] Smart, Lucinda J., Brady J. Engle, Leonard J. Bond, John MacKenzie, and Greg Morris. "Material Characterization of Pipeline Steels: Inspection Techniques Review and Potential Property Relationships." In 2016 11th International Pipeline Conference, pp. V003T05A023-V003T05A023. American Society of Mechanical Engineers, 2016.

[4] Liu S, Sun Y, Gu M, Liu C, He L, Kang Y. Review and analysis of three representative electromagnetic NDT methods. Insight-Non-Destructive Testing and Condition Monitoring. 2017;59(4):176-183.

[5] Sophian A, Tian GY, Taylor D, Rudlin J. Electromagnetic and eddy current NDT: a review. Insight. 2001;43(5):302-6.

[6] García-Martín J, Gómez-Gil J, Vázquez-Sánchez E. Non-destructive techniques based on eddy current testing. Sensors. 2011;11(3):2525-2565.

[7] Abidin IZ, Tian GY, Wilson J, Yang S, Almond D. Quantitative evaluation of angular defects by pulsed eddy current thermography. NDT & E International. 2010;43(7):537-546.

[8] Chen Z, Yusa N, Miya K. Enhancements of eddy current testing techniques for quantitative nondestructive testing of key structural components of nuclear power plants. Nuclear

Engineering and Design. 2008;238(7):1651-1656.

[9] Alobaidi WM, Alkuam EA, Al-Rizzo HM, Sandgren E. Applications of ultrasonic techniques in oil and gas pipeline industries: a review. American Journal of Operations Research. 2015;5(04):274-287.

[10] Li J, Rose JL. Angular-profile tuning of guided waves in hollow cylinders using a circumferential phased array. IEEE Transactions on Ultrasonics, Ferroelectrics, and Frequency Control. 2002;49(12):1720-1729.

[11] Tua PS, Quek ST, Wang Q. Detection of cracks in cylindrical pipes and plates using piezo-actuated Lamb waves. Smart Materials and Structures. 2005;14(6):1325-1342.

[12] Salzburger HJ, Niese F, Dobmann G. EMAT pipe inspection with guided waves. Welding in the world. 2012;56(5-6):35-43.

[13] Sugawara K, Hashizume H, Kitajima S. Development of NDT method using electromagnetic waves. JSAEM Studies in Applied Electromagnetics & Mechanics. 2001;10:313-316.

[14] Hashizume H, Shibata T, Yuki K. Crack detection method using electromagnetic waves. International Journal of Applied Electromagnetics and Mechanics. 2004;20(3, 4):171-178.

[15] Shibata T, Hashizume H, Kitajima S, Ogura K. Experimental study on NDT method using electromagnetic waves. Journal of Materials Processing Technology. 2005;161(1-2):348-352.

[16] Jones RE, Simonetti F, Lowe MJ, Bradley IP. Use of microwaves for the detection of water as a cause of corrosion under insulation. Journal of Nondestructive Evaluation. 2012;31(1):65-76.

[17] Liu L, Ju Y. A high-efficiency nondestructive method for remote detection and quantitative

evaluation of pipe wall thinning using microwaves. NDT & E International. 2011;44(1):106-110.

[18] Liu L, Ju Y, Chen M, Fang D. Application of microwaves for nondestructive and high-efficiency detection of wall thinning locations in a long-distance metal pipe. Materials Transactions. 2011;52(11):2091-2097.

[19] Liu L, Ju Y, Chen M. Optimizing the frequency range of microwaves for high-resolution evaluation of wall thinning locations in a long-distance metal pipe. NDT & E International. 2013; 57:52-57.

[20] Sasaki K, Katagiri T, Yusa N, Hashizume H. Experimental verification of long-range microwave pipe inspection using straight pipes with lengths of 19–26.5 m. NDT & E International. 2018;96:47-57.

[21] Sasaki K, Katagiri T, Yusa N, Hashizume H. Demonstration of the Applicability of Nondestructive Microwave Testing to the Long-Range Inspection of Inner-Surface Cracks in Tubes. Materials Transactions. 2017;58(4):692-6.

[22] Katagiri T, Sasaki K, Song H, Yusa N, Hashizume H. Proposal of a TEM to TE 01 mode converter for a microwave nondestructive inspection of axial flaws appearing on the inner surface of a pipe with an arbitrary diameter. International Journal of Applied Electromagnetics and Mechanics. 2018;59:1–8.

[23] Sasaki K, Development of Long-range Nondestructive Testing Technology Using Microwave for Defects in Pipes, Doctoral dissertation, Tohoku University, 2016.

[24] Yang S, Li H. Optimization of novel high-power millimeter-wave TM_{01}-TE_{11} mode converters. IEEE Transactions on Microwave Theory and Techniques. 1997;45(4):552-554.

[25] Ling GS, Zhou JJ. Design of mode converters for generating the TE11 mode from TM01 vircator at 4GHz. International Journal of Electronics. 2003;89(12):925-930.

[26] Yuan CW, Zhong HH, Qian BL. Tri-bend TM01-TE11 mode converter with input-output aligned on the same axis. High Power Laser and Particle Beams. 2006;18(11):1864-1868.

[27] Niu XJ, Zhu XN, Liu YH, Yu XH, Li HF. Study of Ka-band TM 01 to TE 11 Mode Converters with Parallel Input and Output Waveguides. Journal of Infrared, Millimeter, and Terahertz Waves. 2014;35(2):179-186.

[28] Gifuni A, Perna S. Analysis on the Calculation of the Inverse Discrete Fourier Transform (IDFT) of Passband Frequency Response Measurements in Terms of Lowpass Equivalent Response. Progress In Electromagnetics Research. 2017;160:63-69.

[29] Keysight Technologies. Time domain analyzer using a network analyzer. Application note 1287-12, Literature number 5989-5723EN, Published in USA, Dec. 2, 2017.

[30] Anritsu. Time Domain Measurements Using Vector Network Analyzers. Application note No. 11410-00722, Rev. A, Printed in United States 2013-08.

[31] Sasaki K, Liu L, Yusa N, Hashizume H. Optimized microwave excitation probe for general application in NDT of wall thinning in metal pipes of arbitrary diameter. NDT & E International. 2015;70:53-59.

[32] Morgan SP. Theory of curved circular waveguide containing an inhomogeneous dielectric. Bell System Technical Journal. 1957 Sep;36(5):1209-1251.

[33] Kumrić H, Thumm M. Optimized overmoded TE01-to-TM11 mode converters for high-power millimeter wave applications at 70 and 140 GHz. International Journal of Infrared and Millimeter Waves. 1986;7(10):1439-1463.

[34] Li H, Thumm M. Mode conversion due to curvature in corrugated waveguides. International Journal of Electronics. 1991;71(2):333-47.

[35] G. Chen, et al. Evaluation of factors influencing modal conversion at bend in the light of pipe inspection using microwave NDT, 6th JSNDI Tohoku Branch Symposium, Japan: Sendai, 2018/04, p.3.

[36] G. Chen, et al. Evaluation of general applicability of microwave NDT to pipes with a bend focusing on mode conversion, 15th Japan Society of Maintenology Conference: Student Session, Japan: Fukuoka, 2018/07, p. 277-280.

[37] Sakai Y, Yusa N, Hashizume H. Nondestructive evaluation of wall thinning inside a pipe using the reflection of microwaves with the aid of signal processing. Nondestructive Testing and Evaluation. 2012;27(2):171-184.

Table captions

Figure captions

Table 1. Parameters and values of theoretical calculation

Parameter	Value (step)
r/D [-]	1 – 8 (0.1)
α [deg.]	0 – 180 (1)
f/f_{cM01} [-]	1.03 – 1.63 (0.01)

Table 2. Longitudinal and circumferential positions of axial and circumferential slits in the pipe

L_S (m) \ Cir. Pos.	A	B	C	D
1.5	axial	circumferential	circumferential	axial
3.5	axial and circumferential			
5.5	circumferential	axial	axial	circumferential

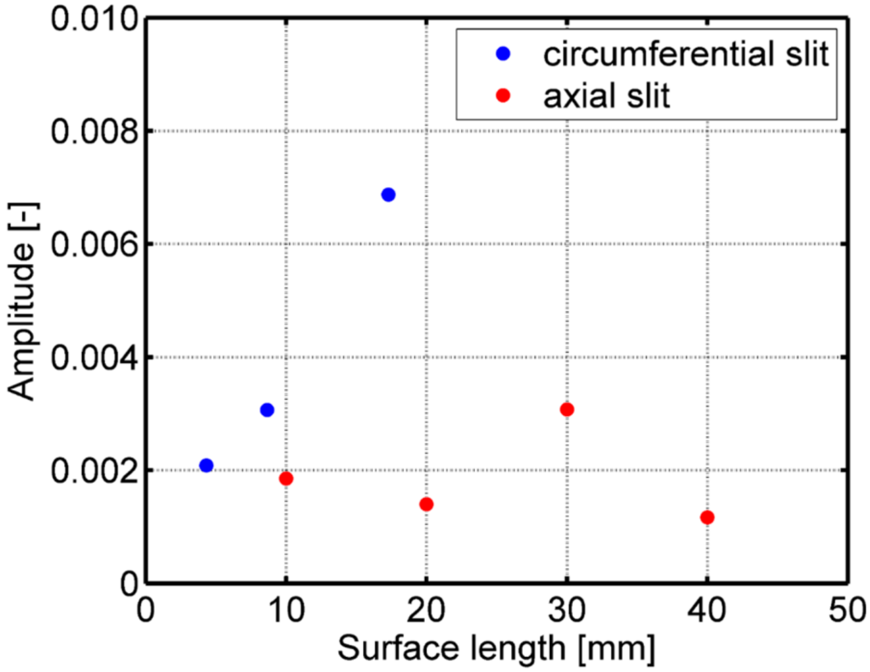

Figure 1. The amplitude of reflection signal against the surface length of the axial/circumferential slit when TM_{01} mode microwaves were used for slit detection.

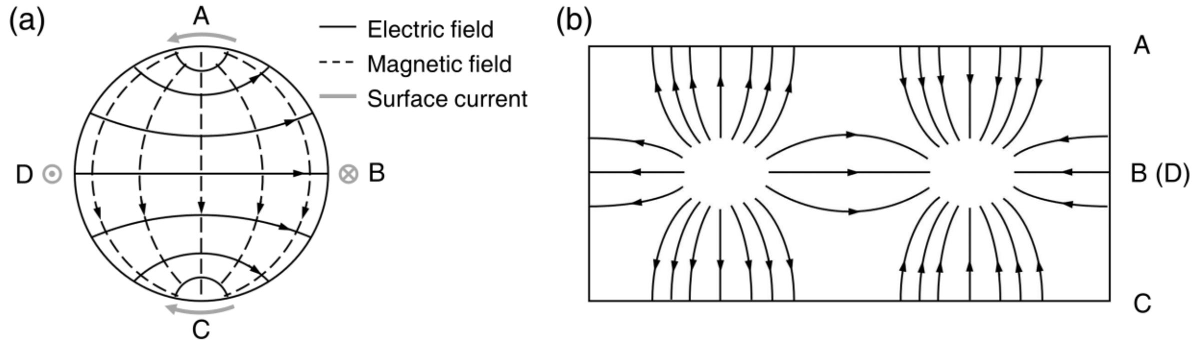

Figure 2. Linearly-polarized circular TE_{11} mode, horizontal polarization, (a) electromagnetic field and surface current, (b) side view of surface current distribution.

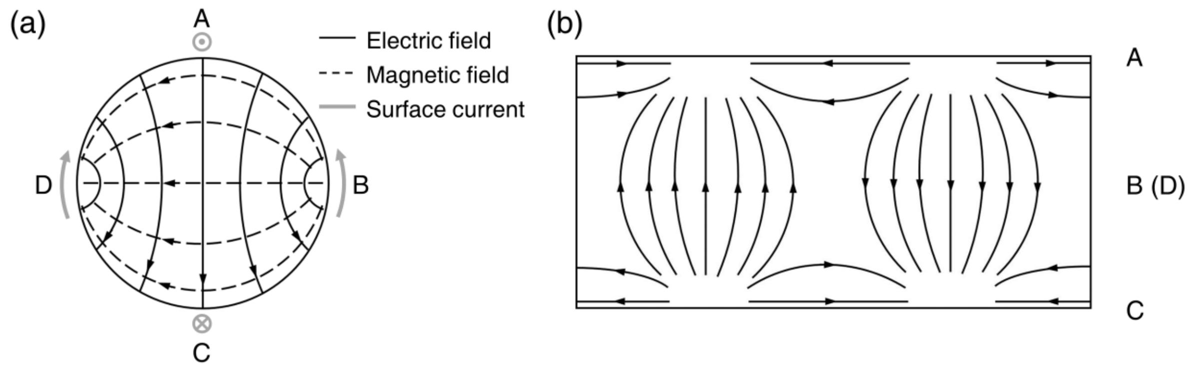

Figure 3. Linearly-polarized circular TE_{11} mode, vertical polarization, (a) electromagnetic field and surface current, (b) side view of surface current distribution.

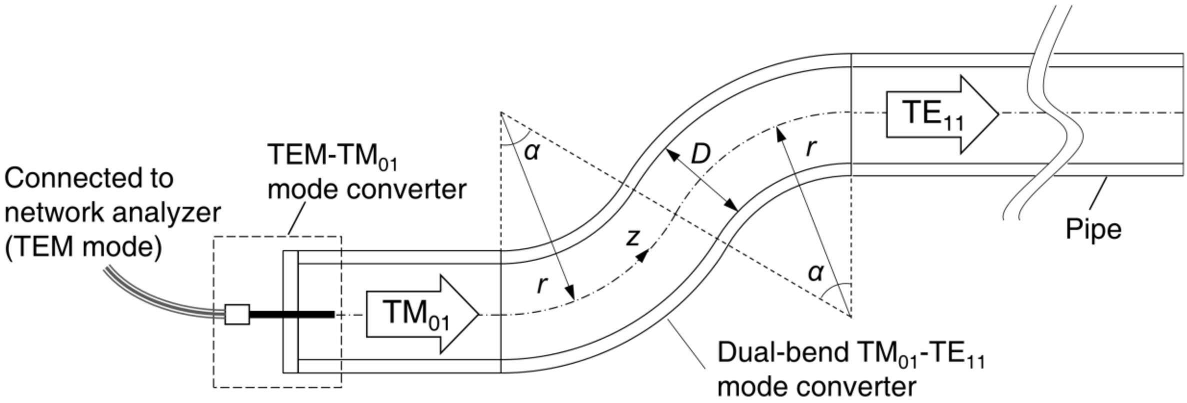

Figure 4. Illustration of the structure of TE_{11} mode converter.

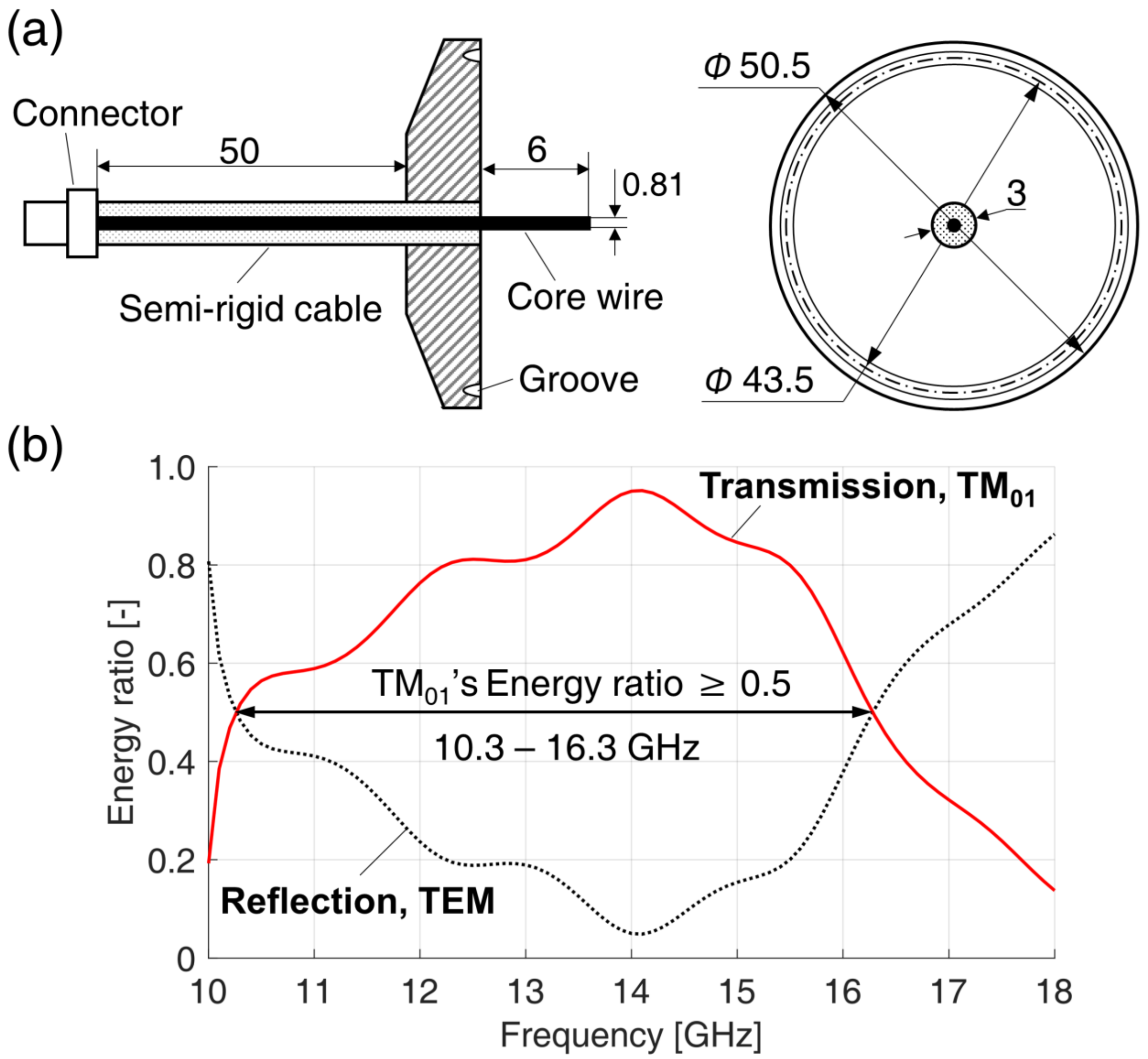

Figure 5. TEM_{01}-TM_{01} mode converter, (a) structure (not to scale), (b) reflection and transmission characteristics.

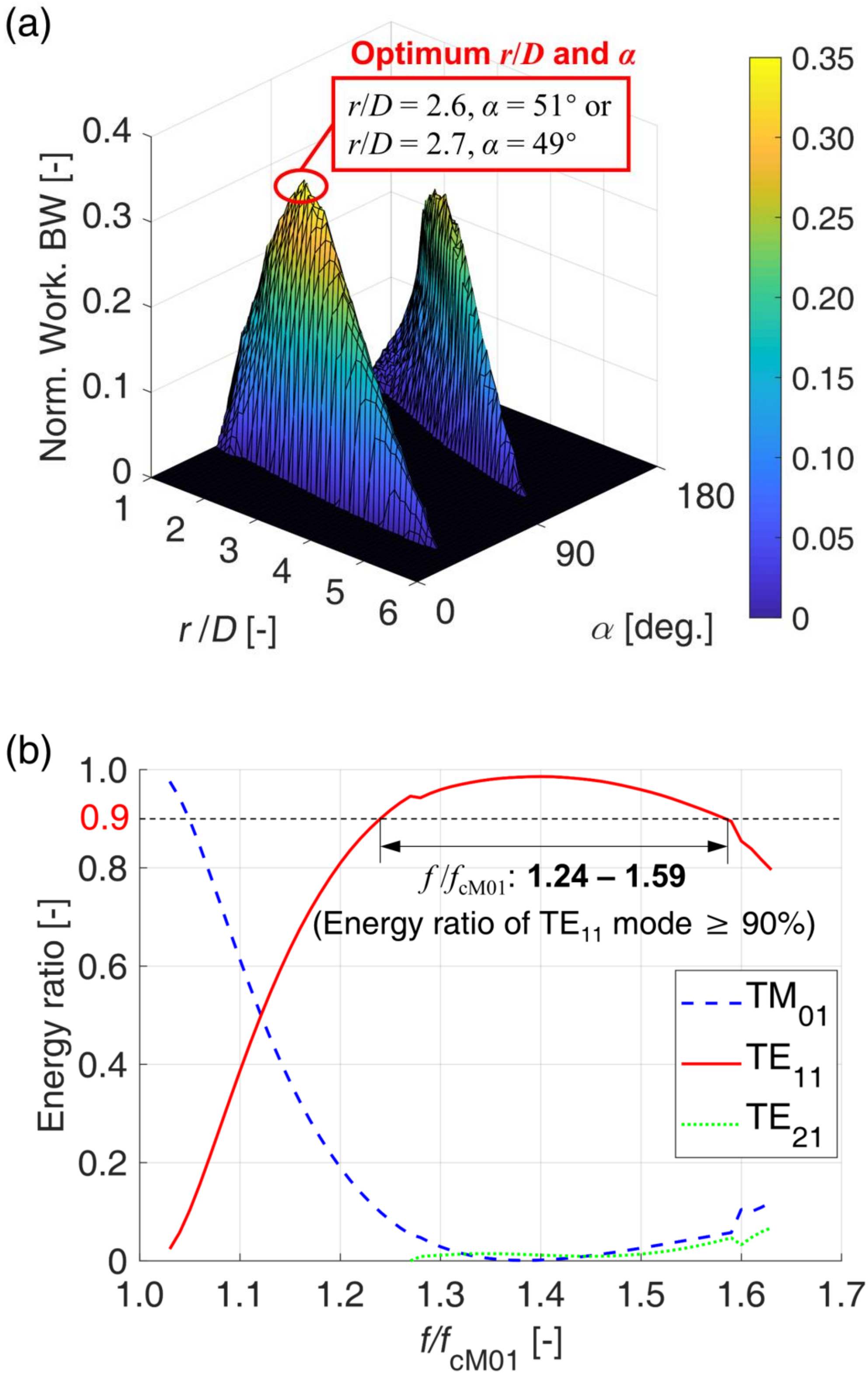

Figure 6. Theoretical calculation of the mode conversion at the TM_{01}-TE_{11} mode converter, (a) normalized working bandwidths of different combinations of r/D and α, (b) fractional energies of different modes versa f/f_{cM01} (r/D =2.6, α =51°).

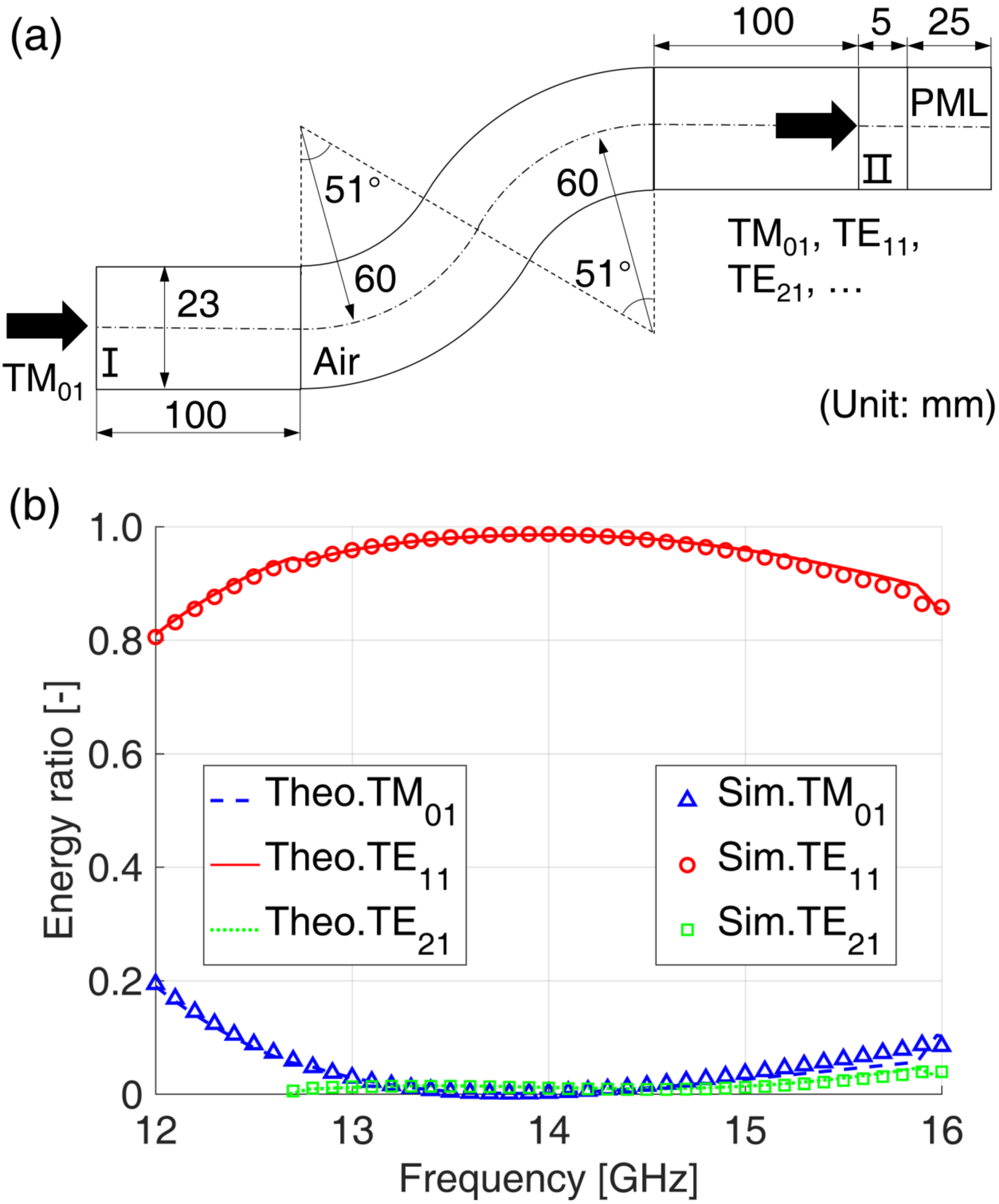

Figure 7. Numerical simulation: (a) geometric model (not to scale), (b) comparison between the result of theoretical calculation and that of numerical simulation (r =60 mm, D =23 mm, α =51°).

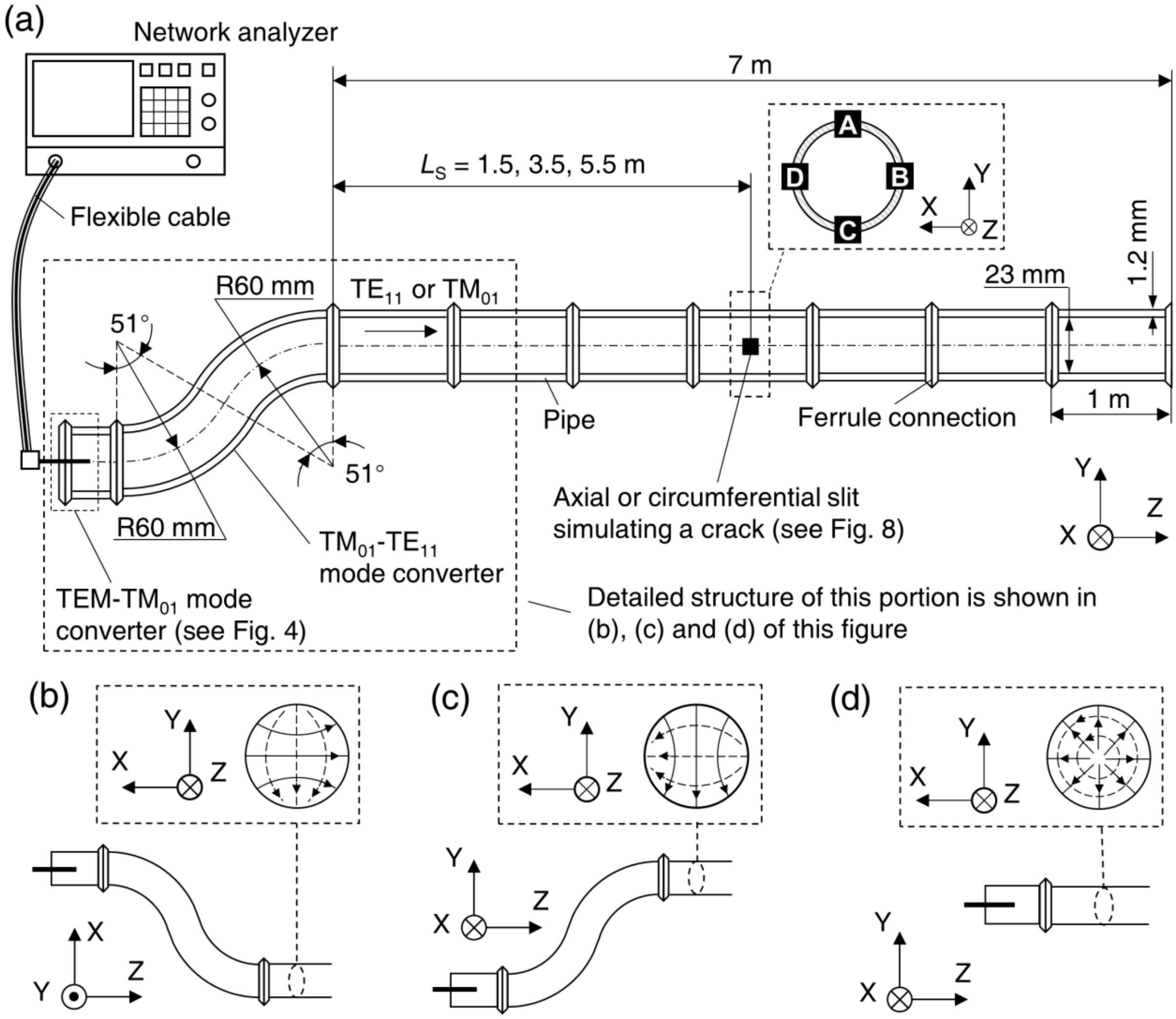

Figure 8. Experimental system (not to scale), (a) Experimental apparatus, (b) generating horizontally-polarized TE_{11} mode, (c) generating vertically polarized TE_{11} mode, (d) generating TM_{01} mode. (**Note:** In (b), (c) and (d), the solid vector-line and broken vector-line in the circular cross-section inside the wireframe are an electric field and a magnetic field, respectively.)

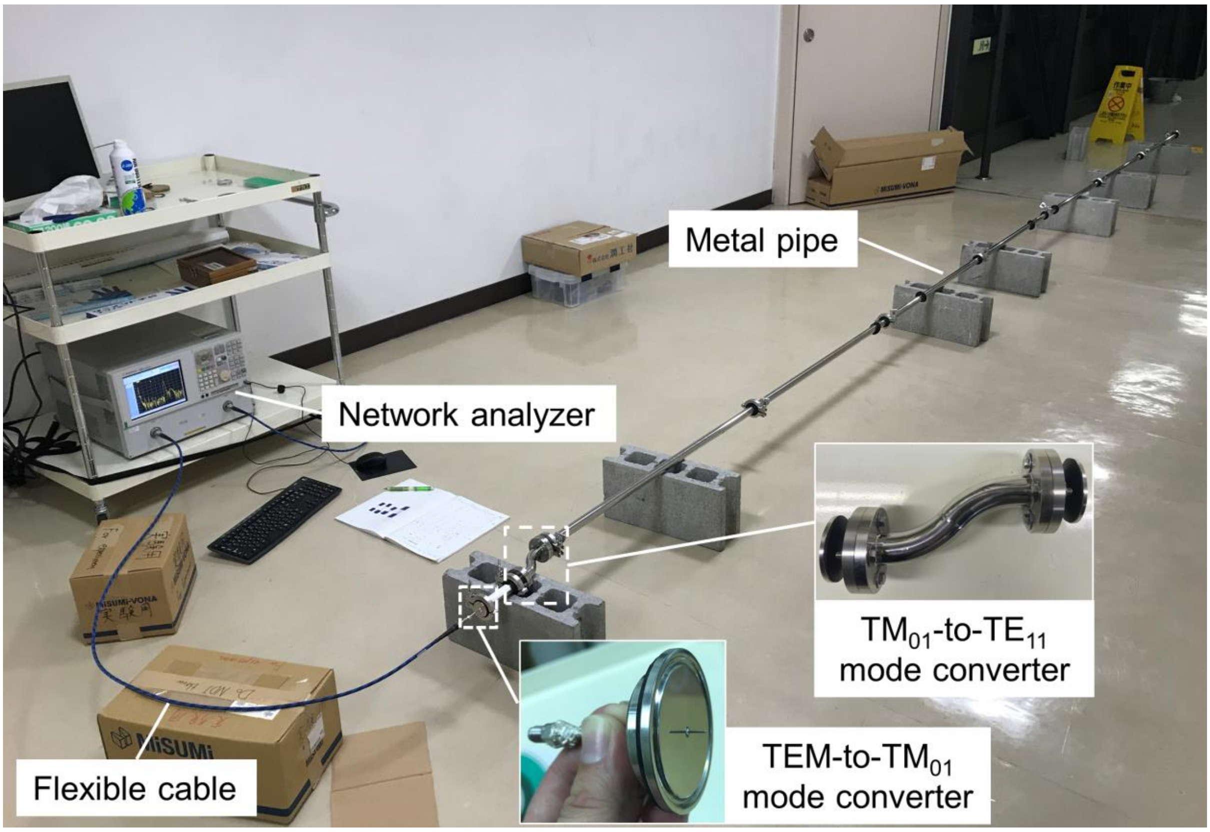

Figure 9. Photo of the experimental setup

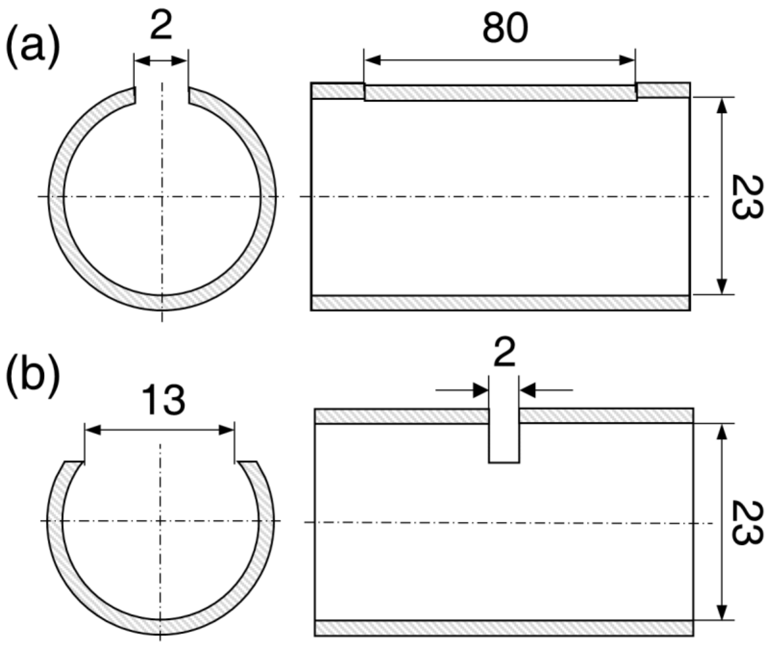

Figure 10. Dimensions of the introduced axial slit and circumferential slit (not to scale), (a) dimensions of the axial slit, (b) dimensions of the circumferential slit.

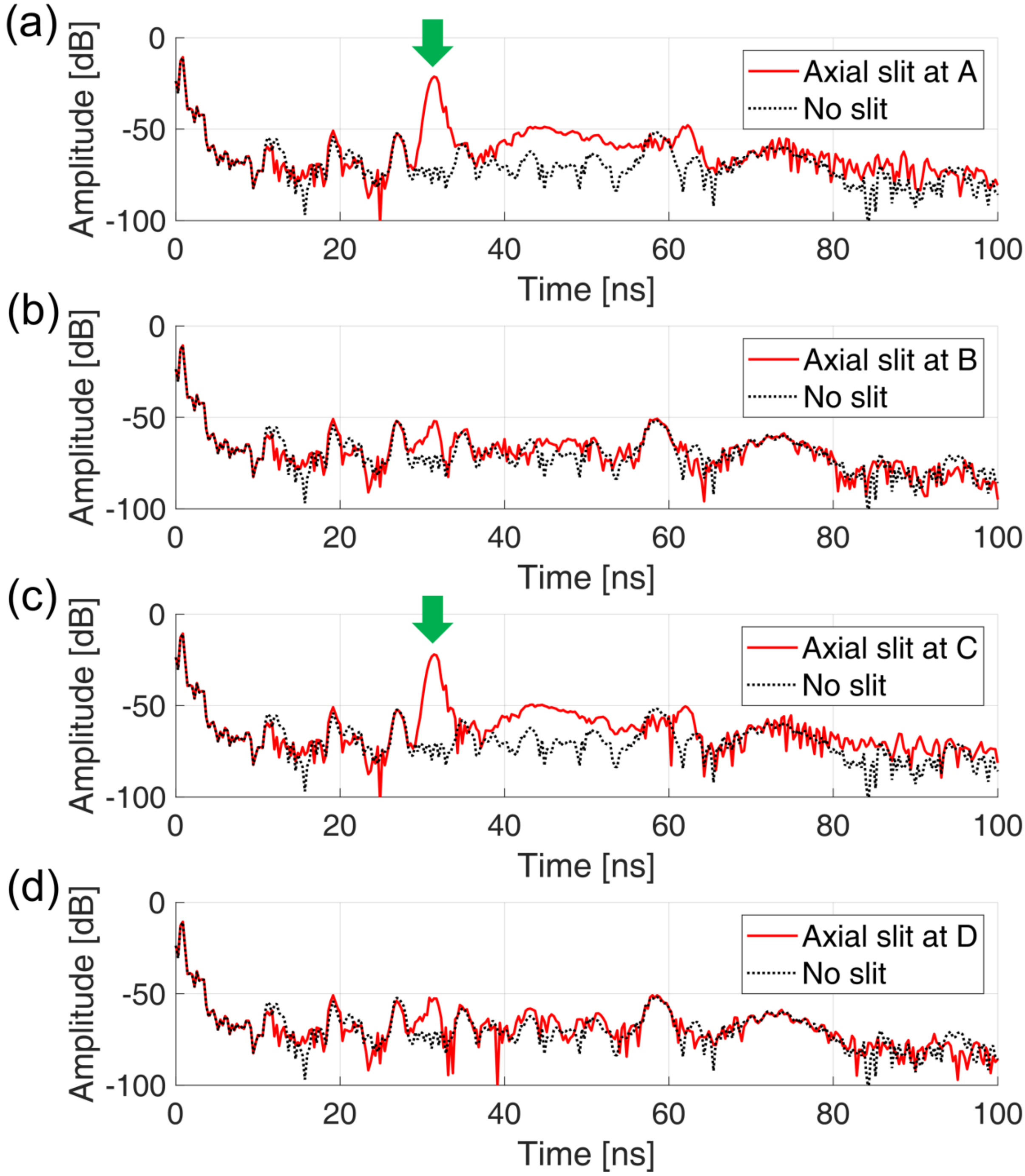
(a)
Amplitude [dB]
Time [ns]
Axial slit at A
No slit
(b)
Amplitude [dB]
Time [ns]
Axial slit at B
No slit
(c)
Amplitude [dB]
Time [ns]
Axial slit at C
No slit
(d)
Amplitude [dB]
Time [ns]
Axial slit at D
No slit

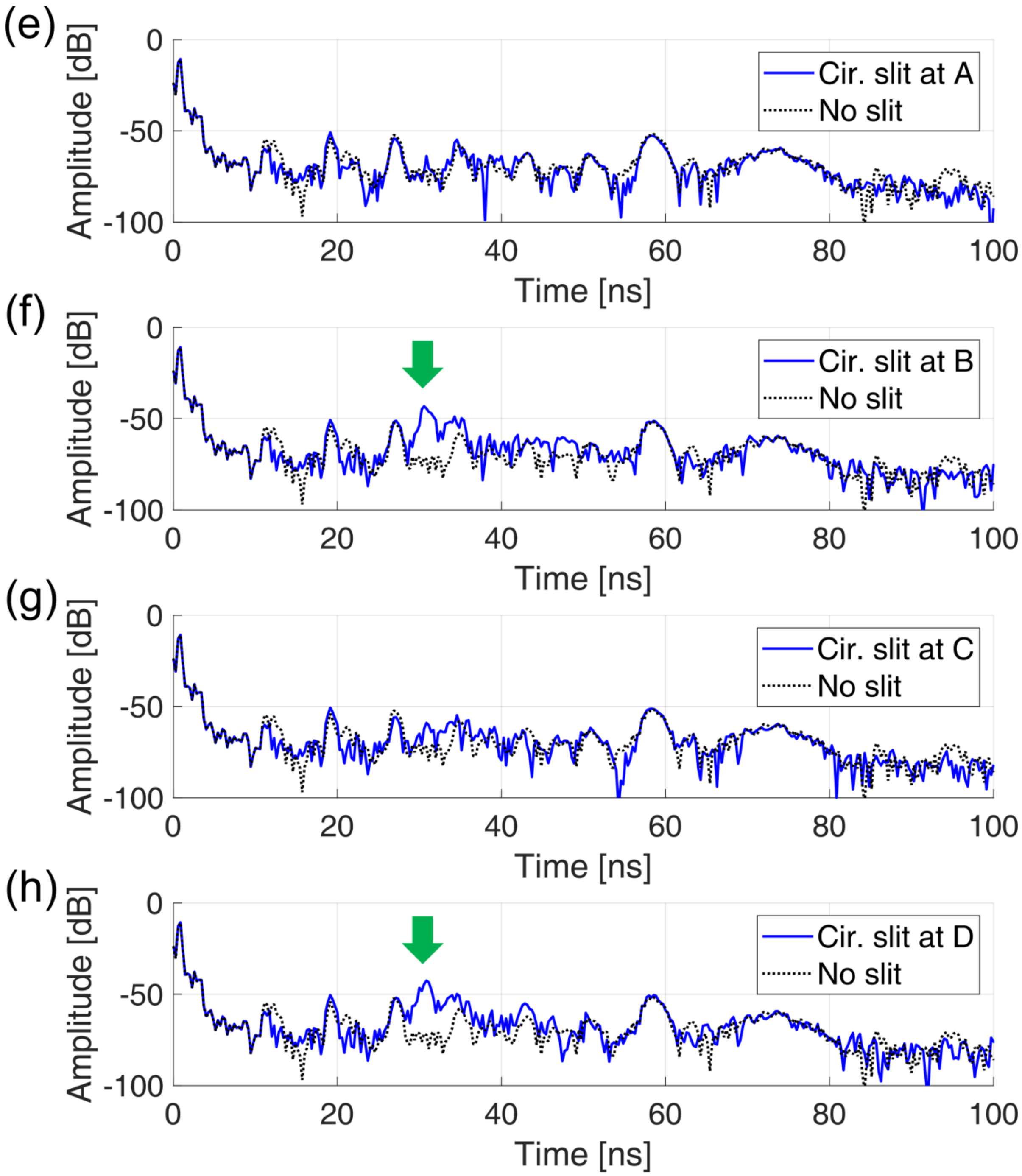

Figure 11. Reflection signals due to slits at L_S=3.5 m, using TE11 mode microwaves of horizontal polarization, (a) – (d) axial slit at points A, B, C and D, (e) – (h) circumferential slit at points A, B, C and D.

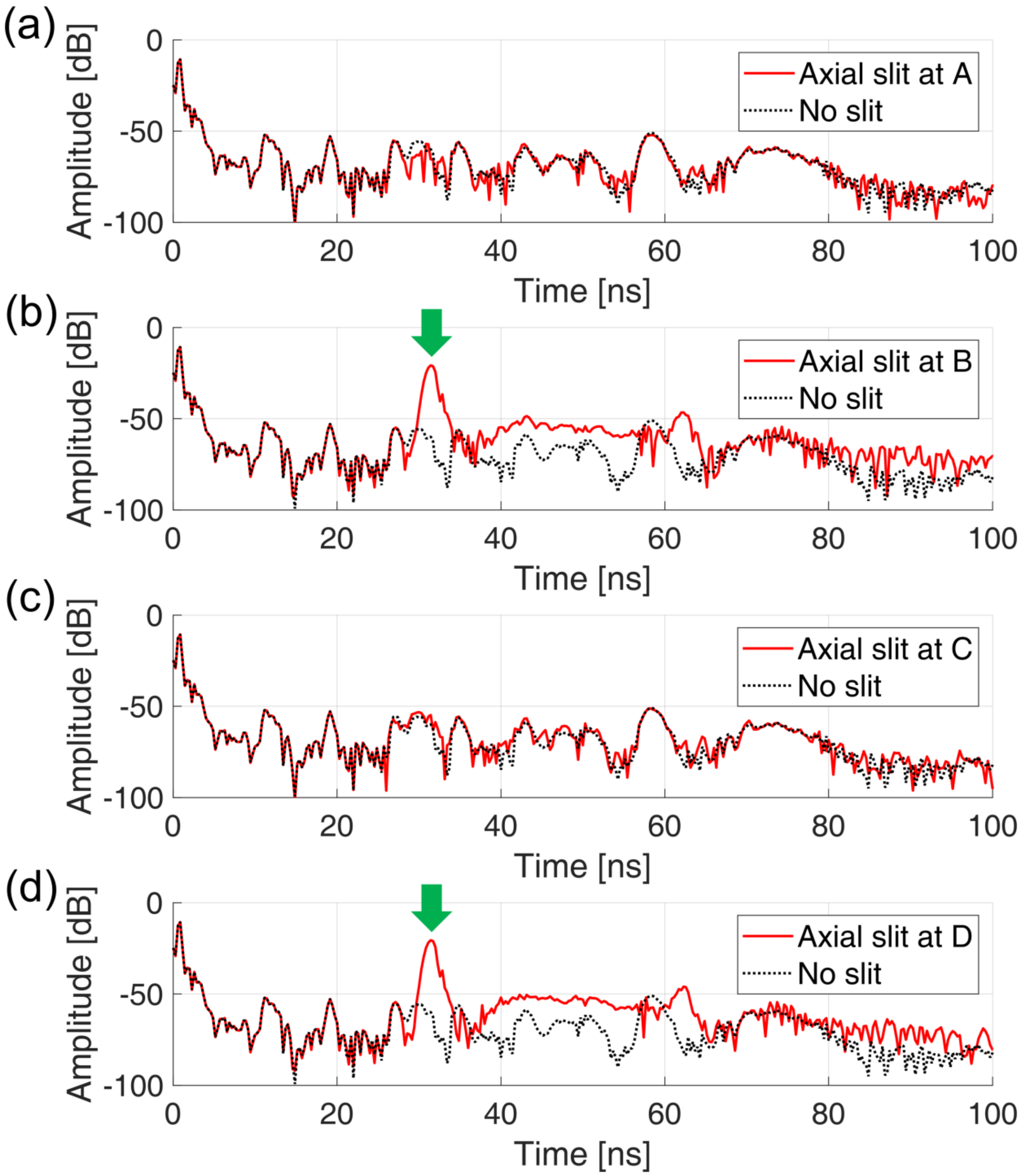
(a)
Amplitude [dB]
0
-50
-100
0
20
40
60
80
100
Time [ns]
Axial slit at A
No slit
(b)
Amplitude [dB]
0
-50
-100
0
20
40
60
80
100
Time [ns]
Axial slit at B
No slit
(c)
Amplitude [dB]
0
-50
-100
0
20
40
60
80
100
Time [ns]
Axial slit at C
No slit
(d)
Amplitude [dB]
0
-50
-100
0
20
40
60
80
100
Time [ns]
Axial slit at D
No slit

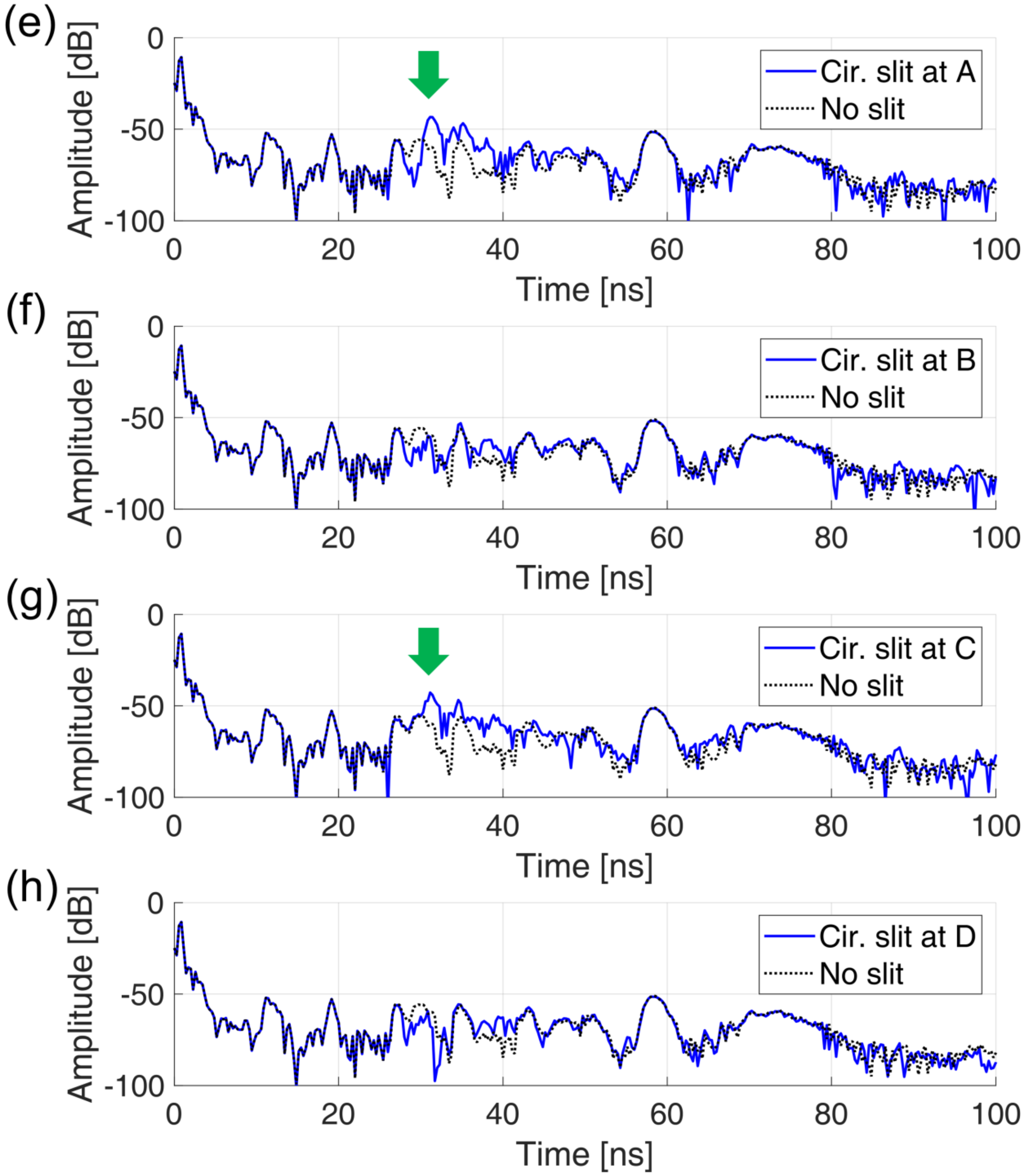

Figure 12. Reflection signals due to slits at L_S=3.5 m, using TE_{11} mode microwaves of vertical polarization, (a) – (d) axial slit at points A, B, C and D, (e) – (h) circumferential slit at points A, B, C and D.

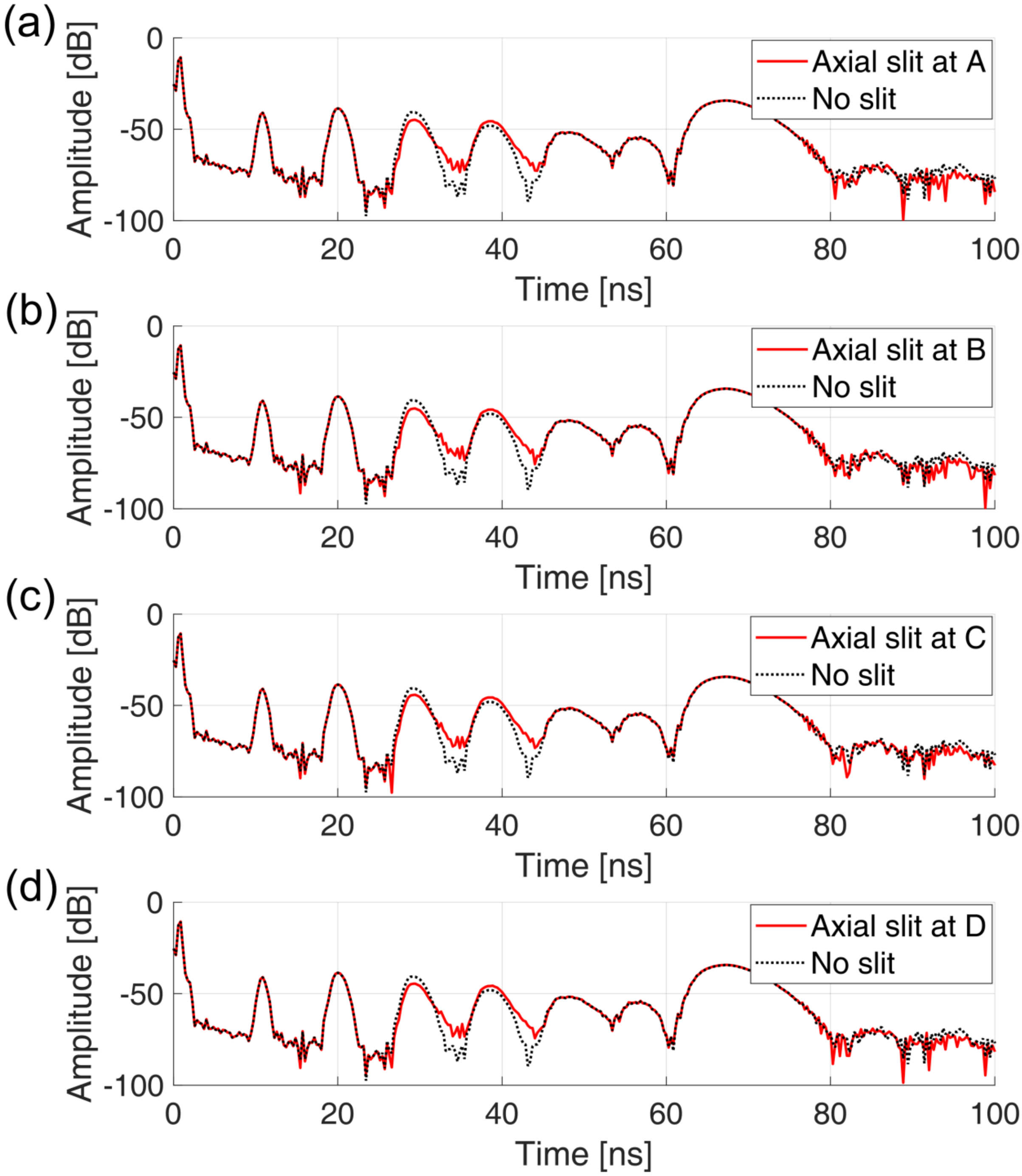
(a)
Amplitude [dB]
0
-50
-100
0
20
40
60
80
100
Time [ns]
Axial slit at A
No slit
(b)
Amplitude [dB]
Axial slit at B
No slit
(c)
Amplitude [dB]
Axial slit at C
No slit
(d)
Amplitude [dB]
Axial slit at D
No slit

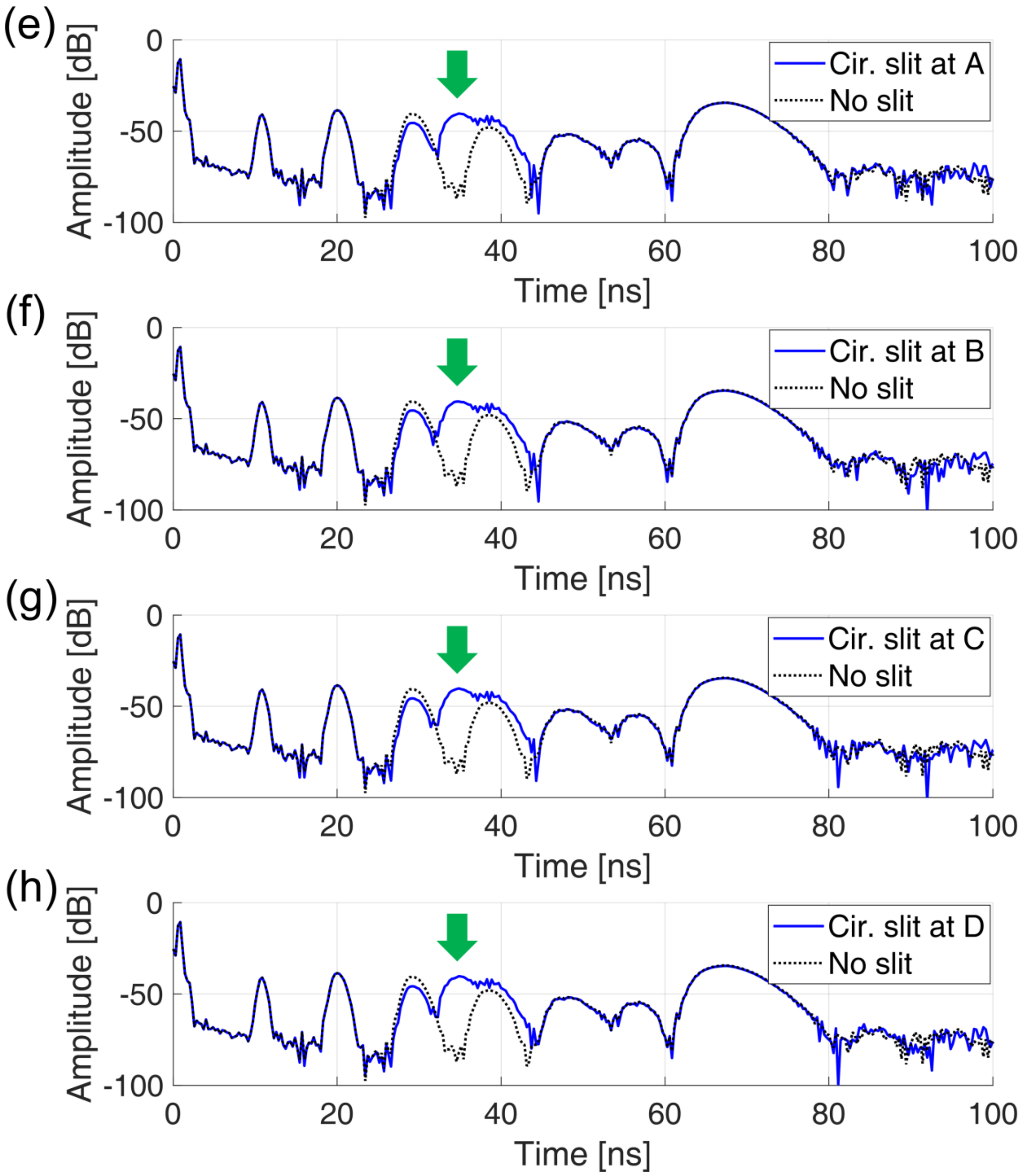

Figure 13. Reflection signals due to slits at L_S=3.5 m, using TM_{01} mode microwaves, (a) – (d) axial slit at points A, B, C and D, (e) – (h) circumferential slit at points A, B, C and D.

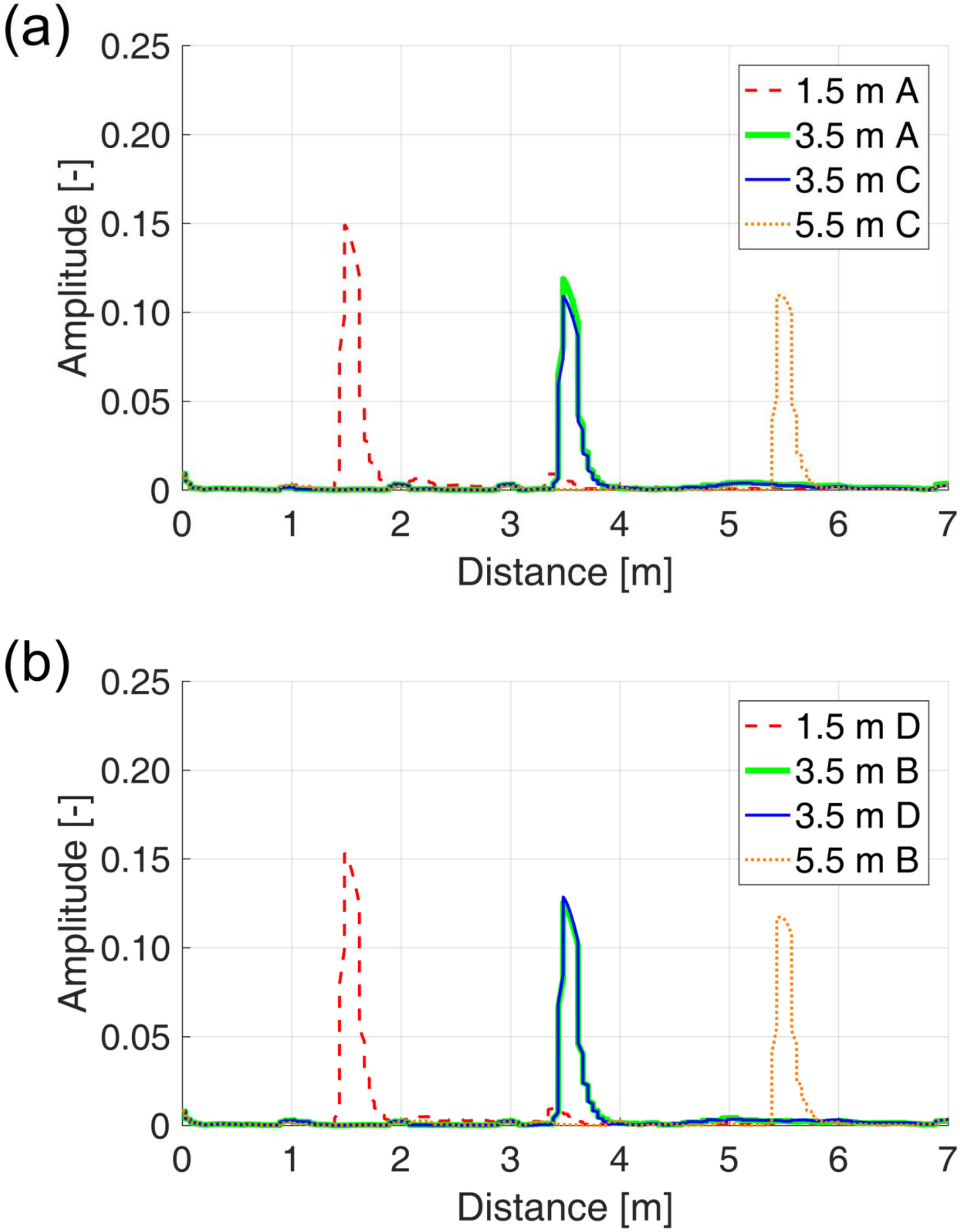

Figure 14. Processed reflection signals of axial slit located at L_S =1.5 m, 3.5 m, 5.5 m and different circumferential positions, using TE_{11} mode microwaves of (a) horizontal polarization, (b) vertical polarization.

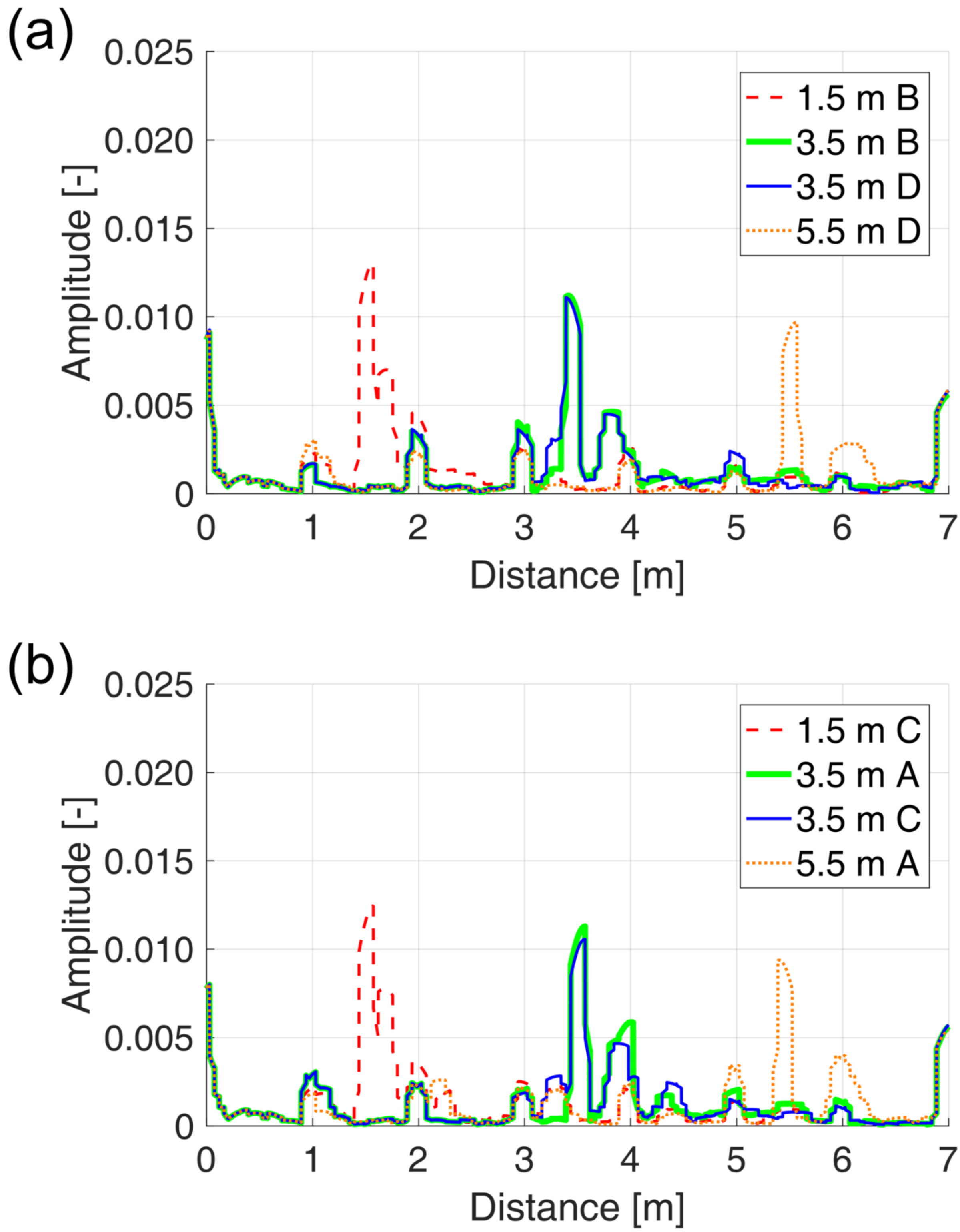

Figure 15. Processed reflection signals of circumferential slit located at L_S =1.5 m, 3.5 m, 5.5 m and different circumferential positions, using TE_{11} mode microwaves of (a) horizontal polarization, (b) vertical polarization.